

# Looking for anomalous $\gamma\gamma H$ and $Z\gamma H$ couplings at future linear colliders

E. Gabrielli <sup>a</sup>, V.A. Ilyin <sup>b</sup> and B. Mele <sup>c</sup>.

<sup>a</sup> Institute of Theoretical Physics, C-XVI, University Autónoma of Madrid, Spain

<sup>b</sup> Institute of Nuclear Physics, Moscow State University, Russia

<sup>c</sup> INFN, Sezione di Roma 1 and Rome University “La Sapienza”, Italy

## Abstract

We consider the possibility of studying anomalous contributions to the  $\gamma\gamma H$  and  $Z\gamma H$  vertices through the process  $e\gamma \rightarrow eH$  at future  $e\gamma$  linear colliders, with  $\sqrt{S} = (500 - 1500)$  GeV. We make a model independent analysis based on  $SU(2) \times U(1)$  invariant effective operators of  $dim = 6$  added to the standard model lagrangian. We consider a light Higgs boson (mostly decaying in  $b\bar{b}$  pairs), and include all the relevant backgrounds. Initial  $e$ -beam polarization effects are also analyzed. We find that the process  $e\gamma \rightarrow eH$  provides an excellent opportunity to strongly constraint both the CP-even and the CP-odd anomalous contributions to the  $\gamma\gamma H$  and  $Z\gamma H$  vertices.

PACS numbers:14.80.Bn, 13.88.+e, 13.60.Hb

e-mail:

emidio.gabrielli@cern.ch, ilyin@theory.npi.msu.su, mele@roma1.infn.it

# 1 Introduction

Higgs boson physics is a major aim in the program of present and future colliders. Presently, direct experimental mass limits on  $m_H$  come from searches at LEP2, giving  $m_H \gtrsim M_Z$ . Also, LEP1 precision measurements consistency sets an upper limit  $m_H \lesssim 300$  GeV in the SM [1].

Once the Higgs boson will be discovered, establishing its properties and interactions will be crucial either to consolidate the standard model (SM) or to find possible anomalies. Indeed, the symmetry breaking sector of the theory is expected to be particularly sensitive to the presence of possible new physics (NP) effects that could eventually even explain its origin.

The interactions of the Higgs boson with the neutral electroweak gauge bosons,  $\gamma$  and  $Z$ , are particularly interesting. By measuring the three vertices  $ZZH$ ,  $\gamma\gamma H$  and  $Z\gamma H$ , one can test a delicate feature of the Standard Model, that is the relation between the spontaneous symmetry-breaking mechanism and the electroweak mixing of the two gauge groups  $SU(2)$  and  $U(1)$ . While the  $ZZH$  vertex occurs at the tree level, the other two contribute only at one loop in the SM. As a consequence the  $\gamma\gamma H$  and  $Z\gamma H$  couplings are particularly sensitive to possible contributions from new physics, such as the existence of new heavy particles circulating in the loop.

A measurement of the  $\gamma\gamma H$  and  $Z\gamma H$  couplings could be performed at LHC, by determining the branching ratio ( $B$ ) of the corresponding Higgs boson decays  $H \rightarrow \gamma\gamma$  and  $H \rightarrow Z\gamma$ . This holds for a rather light Higgs, i.e.  $m_H \lesssim 140$  GeV [ $(m_H \gtrsim 115$  GeV is also required in the latter channel, which guarantees a  $B(H \rightarrow Z\gamma)$  as large as  $\mathcal{O}(10^{-3})$ ]. Measuring the  $Z\gamma H$  vertex is anyhow more complicated. The  $H \rightarrow Z\gamma$  final states include the  $Z$  decay products, either jets or lepton pairs, for which much heavier backgrounds are expected.

A more accurate determination of both the  $\gamma\gamma H$  and  $Z\gamma H$  vertices is expected at future linear colliders with c.m. energy  $\sqrt{s} \simeq (300 \div 2000)$  GeV and integrated luminosity  $\mathcal{O}(100 \div 1000)$  fb $^{-1}$  [2, 3]. Besides  $e^+e^-$  collisions, linear colliders give the possibility, through laser backscattering [4, 5], to study  $\gamma\gamma$  and  $\gamma e$  interactions at energies and luminosities comparable to those in  $e^+e^-$  collisions. While the process  $\gamma\gamma \rightarrow H$  on the Higgs boson resonance will be the ideal place where to measure the  $\gamma\gamma H$  coupling, the reaction  $e\gamma \rightarrow eH$  will give a unique possibility to study both the  $\gamma\gamma H$  (without requiring a fine tuning of the c.m. energy, as for the process  $\gamma\gamma \rightarrow H$ ) and  $Z\gamma H$  vertices with good statistics. In fact, the crossed channel  $e^+e^- \rightarrow \gamma H$  suffers from very low cross sections and overwhelming backgrounds [6, 7, 8]. On the other hand, in the channel  $e^+e^- \rightarrow ZH$  also involving the  $Z\gamma H$  coupling, the latter contributes to the corresponding one-loop corrections in the SM, thus implying a large tree-level background over which to study possible small deviations.

In the SM, the one-loop process  $e\gamma \rightarrow eH$  was analysed in details [9], stressing the unique possibility offered by this channel to study the  $Z\gamma H$  coupling in a clear experimental environment and with good statistics. In particular in [9], we remarked how requiring large transverse momentum events automatically selects more efficiently the  $Z\gamma H$  contributions with respect to

the  $\gamma\gamma H$  interaction that is dominant in the total cross section.

In this paper we analyze the prospects of the  $e\gamma \rightarrow eH$  reaction in setting experimental bounds on the value of the anomalous  $\gamma\gamma H$  and  $Z\gamma H$  couplings. Some preliminary results have been presented in [10]\*. We adopt a model independent approach, where an effective lagrangian is obtained by adding  $dim = 6$   $SU(2) \times U(1)$  invariant operators to the SM Lagrangian. In realistic models extending the SM, these operators contribute in some definite combinations. However, this approach can give some general insight into the problem when discussing possible deviations from the standard-model one-loop Higgs vertices. The anomalous operators we will consider contribute to the three vertices  $\gamma\gamma H$ ,  $Z\gamma H$  and  $ZZH$ , only the first two being involved in the  $e\gamma \rightarrow eH$  reaction. Although the anomalous contributions to the  $\gamma\gamma H$  vertex can be more efficiently bounded through the resonant  $\gamma\gamma \rightarrow H$  reaction, independent interesting bounds can be obtained by measuring the total rate of the  $e\gamma \rightarrow eH$  process. On the other hand, the latter channel offers a unique possibility to bound anomalous  $Z\gamma H$  couplings too, the latter being enhanced in large  $p_T$  events. Some general analysis of the potential of the two processes above in bounding the  $\gamma\gamma H$  and  $Z\gamma H$  vertices has been given in [11]. Here we provide a more detailed study of the process  $e\gamma \rightarrow eH$  at c.m. energies of 500 and 1500 GeV, when the Higgs boson decays predominantly in  $b$ -quark pairs, (i.e. for  $m_H \lesssim 140$  GeV) that includes all the relevant backgrounds and initial beam polarization effects.

We stress that in our analysis we assume a monochromatic photon beam. Presently<sup>†</sup>, experts on photon-beams construction in  $e^+e^-$  colliders claim that assuming a particular form for the photon beam energy spectrum (as is often done in the literature) is somewhat premature. According to what it is actually known, it seems *cleaner*, as far as predictions are concerned, to simply assume a monochromatic photon beam with an energy equal to the expected peak energy of the laser backscattered photons, which is about 0.8 times the energy of the basic electron beam. This, for instance, gives  $e\gamma$  collisions with  $\sqrt{s} = 0.9$  TeV, when starting from a  $e^+e^-$  colliders at  $\sqrt{s} = 1$  TeV. Regarding the luminosity of the  $e\gamma$  machine, this is presently expected to be comparable with the luminosity of the initial  $e^+e^-$  machine (the most pessimistic assumptions gives a reduction factor of about 1/3 with respect to the corresponding  $e^+e^-$  machine).

The paper is organized as follows. In section 2, we summarize the  $e\gamma \rightarrow eH$  process main features in the SM. We then review the channels that give important backgrounds for the  $e\bar{b}\bar{b}$  final state. In section 3, we introduce the effective lagrangian describing the relevant anomalous interactions and give the analytical expressions for the corresponding helicity amplitudes for the process  $e\gamma \rightarrow eH$ . In section 4 we discuss our strategy for getting bounds on the anomalous  $\gamma\gamma H$  and  $Z\gamma H$  couplings from  $e\gamma \rightarrow eH$ . We describe the kinematical cuts that optimize the signal to background ratio ( $S/B$ ), including the SM signal among the “backgrounds”. Sections 5 contains our numerical results. In section 6, we discuss the resulting limits that can be put

---

\*Note that in this talk the factor  $(-g_e^\sigma)$  (the  $Z$  charge of electron) is missing in the formula for the anomalous contribution to the amplitude.

<sup>†</sup>We acknowledge thorough and enlightening discussions with V. Telnov on this point.

on the New Physics (NP) scale  $\Lambda$  and give our conclusions <sup>‡</sup>.

## 2 The reaction $e\gamma \rightarrow eH$ in the SM and other background channels

In this section we describe the main channels that contribute as backgrounds in the search for anomalous couplings through the process  $e\gamma \rightarrow eH$  followed by the Higgs boson decay  $H \rightarrow b\bar{b}$ . We first summarize the main feature of the  $e\gamma \rightarrow eH$  process in the SM, that, in a sense, is the first “irreducible” background to be taken into account when searching for an anomalous signal.

In [9], we presented the complete analytical results for the helicity amplitudes of the  $e\gamma \rightarrow eH$  process (see also [13]). This amplitude is given in terms of the contributions denoted as ‘ $\gamma\gamma H$ ’ and ‘ $Z\gamma H$ ’, which are related to the  $\gamma\gamma H$  and  $Z\gamma H$  vertices respectively, and a ‘BOX’ contribution. The separation of the rate into these three parts corresponds to the case where the Slavnov-Taylor identities for the ‘ $\gamma\gamma H$ ’ and ‘ $Z\gamma H$ ’ Green functions just imply the transversality with respect to the incoming photon momentum (see also [11] for a detailed discussion of this formally delicate separation).

The total rate of this reaction is rather large. In particular, if  $\sqrt{s} \gtrsim 500$  GeV, one finds  $\sigma > 10$  fb for  $m_H$  up to about 250 GeV, and  $\sigma > 1$  fb for  $m_H$  up to about 400 GeV. In the total cross section, the main contribution is given by the  $\gamma\gamma H$  vertex because of the massless photon propagator in the  $t$ -channel. On the other hand, the  $Z\gamma H$  vertex contribution is depleted by the  $Z$  propagator in the  $t$ -channel. As discussed in [9] and [11], the  $Z\gamma H$  vertex effects can then be enhanced by requiring a final electron tagged at large angle. Indeed, the latter kinematical configuration strongly depletes the photon propagator and, hence, the  $\gamma\gamma H$  vertex contribution, while keeping most of the  $Z\gamma H$  contribution. For example, for  $p_T^e > 100$  GeV and  $\sqrt{s} \simeq 500$  GeV, we found that the  $Z\gamma H$  contribution to the cross section is about 60% of the  $\gamma\gamma H$  one, hence giving a considerable fraction of the production rate, that, at the same time, is still sufficient to guarantee investigation (about 0.7 fb for  $m_H \sim 120$  GeV).

In what follow, we will consider also the possibility of having longitudinally polarized electron beams. In [9], we studied, for  $m_H = 120$  GeV, the  $e$ -beam polarization dependence of the SM total cross section and of its  $\gamma\gamma H$ ,  $Z\gamma H$  and BOX components, and their interference pattern. The latter turns out to be particularly sensitive to the electron polarization. For instance, assuming left-handed electrons with  $P_e = -1$  (right-handed electrons with  $P_e = +1$ ) the total cross section increases (decreases) by about 94% at  $\sqrt{s} = 500$  GeV. Indeed, for  $P_e = -1$  ( $P_e = +1$ ), there is a strong constructive (destructive) interference between the  $\gamma\gamma H$  and  $Z\gamma H$  contributions to the amplitude.

Apart from the SM signal in  $e\gamma \rightarrow eH$ , the relevant backgrounds in our problem are

---

<sup>‡</sup>Most of the results presented in this work were obtained with the help of the CompHEP package [12].

all the background channels analyzed in [9] for the SM  $e\gamma \rightarrow eH \rightarrow ebb\bar{b}$  process. The main irreducible background comes from the direct production of  $b$ -quark pairs in  $e\gamma \rightarrow ebb\bar{b}$ . An angular cut on the  $b$ 's with respect to both the beams can reduce the rate for this potentially dangerous background to a comparable level with the SM signal. Also, whenever the  $c$  quarks are misidentified into  $b$ 's, a further source of background is given by the charm-pair production through  $e\gamma \rightarrow e c\bar{c}$ . Assuming about 10% of probability of misidentifying a  $c$  quark into a  $b$ , the contribution of the  $e\gamma \rightarrow e c\bar{c}$  “effective rate” turns out to be of the same order as the  $e\gamma \rightarrow ebb\bar{b}$  rate.

A further background, analyzed in [9], is the resolved  $e\gamma(g) \rightarrow ebb\bar{b}(ec\bar{c})$  production, where the photon interacts via its gluonic content. This was found to be negligible with respect to the previous channels.

At moderate values of  $\sqrt{s}$  ( $\sqrt{s} \sim 500$  GeV), further improvements in the  $S/B$  ratio can be obtained by exploiting the final-electron angular asymmetry in the SM signal [9]. Indeed, the final electron in  $e\gamma \rightarrow eH$  moves mostly in the forward direction. On the other hand, for the  $e\gamma \rightarrow ebb\bar{b}$  background the final electron angular distribution, although not completely symmetric, is almost equally shared in the forward and backward direction with respect to the beam. On the other hand, for  $\sqrt{s} \gtrsim 1$  TeV, a clear asymmetry develops in the background channel too. In fact, the contribution of the diagrams with an electron exchanged in the  $u$ -channel (responsible for the backscattering of final electrons) decreases as  $1/s$ . Hence, at large  $\sqrt{s}$ , one does not get improvements in the  $S/B$  ratio by exploiting this forward-backward asymmetry. Anyhow, even at lower values of  $s$ , although the  $S/B$  ratio can be improved up to  $\sim 1$ , the bounds discussed below depend only marginally on the electron angular cut.

After a detailed study of the SM signal versus all the relevant backgrounds, in [9] we concluded that with a luminosity of  $100 \text{ fb}^{-1}$ , at  $\sqrt{s} = 500$  GeV, one expects an accuracy as good as about 10% on the measurement of the  $Z\gamma H$  effects, assuming the validity of the SM. Here, we will use a similar strategy to study the sensitivity of the  $e\gamma \rightarrow eH$  process to possible anomalous coupling contributions in both the  $\gamma\gamma H$  and  $Z\gamma H$  vertices.

### 3 The effective Lagrangian

In our study, we want to set the sensitivity of the  $e\gamma \rightarrow eH$  process to possible anomalies in the  $\gamma\gamma H$  and  $Z\gamma H$  interactions in a most general framework. To this end, we adopt the effective Lagrangian formalism [14] that is able to describe the low-energy residual effects of some complete theory correctly describing NP at higher energy scales. This introduces  $dim = 6$   $SU(2) \times U(1)$  invariant operators. Among the different operators involving the Higgs boson, the ones contributing to the  $e\gamma \rightarrow eH$  amplitude via anomalous couplings in the  $\gamma\gamma H$  and  $Z\gamma H$  vertices are particularly interesting here. We then will concentrate on the so-called “superblind” operators, that is the ones not leading at the same time to anomalous gauge-boson self couplings that can be more comfortably constrained in processes like  $e^+e^- \rightarrow WW$ .

In particular, assuming the so-called custodial symmetry, two pairs (the first CP-even and the second CP-odd) of effective operators are relevant for our problem

$$\mathcal{L}^{eff} = d \cdot \mathcal{O}_{UW} + d_B \cdot \mathcal{O}_{UB} + \bar{d} \cdot \bar{\mathcal{O}}_{UW} + \bar{d}_B \cdot \bar{\mathcal{O}}_{UB}, \quad (1)$$

$$\mathcal{O}_{UW} = \frac{1}{v^2} \left( |\Phi|^2 - \frac{v^2}{2} \right) \cdot W^{i\mu\nu} W_{\mu\nu}^i, \quad \mathcal{O}_{UB} = \frac{1}{v^2} \left( |\Phi|^2 - \frac{v^2}{2} \right) \cdot B^{\mu\nu} B_{\mu\nu}, \quad (2)$$

$$\bar{\mathcal{O}}_{UW} = \frac{1}{v^2} |\Phi|^2 \cdot W^{i\mu\nu} \tilde{W}_{\mu\nu}^i, \quad \bar{\mathcal{O}}_{UB} = \frac{1}{v^2} |\Phi|^2 \cdot B^{\mu\nu} \tilde{B}_{\mu\nu}, \quad (3)$$

where  $\tilde{W}_{\mu\nu}^i = \epsilon_{\mu\nu\mu'\nu'} \cdot W^{i\mu'\nu'}$  and  $\tilde{B}_{\mu\nu} = \epsilon_{\mu\nu\mu'\nu'} \cdot B^{\mu'\nu'}$ . In these formulas  $\Phi$  is the Higgs doublet and  $v$  is the electroweak vacuum expectation value.

Accordingly, the  $\gamma\gamma H$  and  $Z\gamma H$  anomalous terms contributions to the helicity amplitudes of  $e\gamma \rightarrow eH$  are given by:

$$M_{anom}(\sigma, \lambda) = M^{\gamma\gamma}(\sigma, \lambda) + M^{\gamma Z}(\sigma, \lambda), \quad (4)$$

where

$$\begin{aligned} M^{\gamma\gamma}(\sigma, \lambda) &= \frac{4\pi\alpha}{M_Z(-t)} \sqrt{-\frac{t}{2}} \{d_{\gamma\gamma}[(u-s) - \sigma\lambda(u+s) - i\bar{d}_{\gamma\gamma}[\lambda(u-s) + \sigma(u+s)]]\}, \\ M^{\gamma Z}(\sigma, \lambda) &= \frac{4\pi\alpha(-g_e^\sigma)}{M_Z(M_Z^2 - t)} \sqrt{-\frac{t}{2}} \{d_{\gamma Z}[(u-s) - \sigma\lambda(u+s) - i\bar{d}_{\gamma Z}[\lambda(u-s) + \sigma(u+s)]]\}. \end{aligned} \quad (5)$$

Here,  $s$ ,  $t$  and  $u$  are the Mandelstam kinematical variables (defined as in [9]),  $\sigma/2 = \pm 1/2$  and  $\lambda = \pm 1$  are the electron and photon helicities, respectively. The  $Z$  charge of electron is denoted as  $g_e^\sigma$ . The anomalous couplings  $d, d_B, \bar{d}, \bar{d}_B$  contribute to the  $\gamma\gamma H$ ,  $ZZH$ , and  $Z\gamma H$  interactions in the combinations

$$\begin{aligned} d_{\gamma\gamma} &= \tan\theta_W d + (\tan\theta_W)^{-1} d_B, & d_{\gamma Z} &= d - d_B \\ d_{ZZ} &= (\tan\theta_W)^{-1} d + \tan\theta_W d_B, \\ \bar{d}_{\gamma\gamma} &= \tan\theta_W \bar{d} + (\tan\theta_W)^{-1} \bar{d}_B, & \bar{d}_{\gamma Z} &= \bar{d} - \bar{d}_B \\ \bar{d}_{ZZ} &= (\tan\theta_W)^{-1} \bar{d} + \tan\theta_W \bar{d}_B, \end{aligned} \quad (6)$$

where  $\theta_W$  is the Weinberg angle. We assume  $\sin^2\theta_W = 0.2247$ <sup>§</sup>. Note that there is no interference between the CP-odd terms (with couplings  $\bar{d}$ ) and any CP-even triangle diagram inducing the  $\gamma\gamma H$  and  $Z\gamma H$  couplings in the SM amplitude, although the interference with the SM box amplitude is nonvanishing. This is due to the real value of the SM amplitude induced by the triangle diagrams for  $M_H < 2M_W$  and  $M_H < 2m_{top}$  (one can neglect contributions of

<sup>§</sup>All the physical parameters of the SM used here are the same as in our paper[9].

light quark loops), while the box diagrams contribute with complex numbers. Since the box contribution to the SM amplitude is rather small, the complete cross section (i.e., the one deriving from the SM Lagrangian and the effective one) depends only marginally on the sign of the CP-odd couplings  $\bar{d}_{\gamma\gamma}$  and  $\bar{d}_{\gamma Z}$ . On the contrary, for the CP-even terms the interference is relevant, and the dependence on the  $d_{\gamma\gamma}$  and  $d_{\gamma Z}$  coupling is not symmetrical with respect to the corresponding SM point ( $d_{\gamma\gamma} = 0$ ,  $d_{\gamma Z} = 0$ ). This effect, generally speaking, decreases the sensitivity to the CP violating anomalous couplings.

## 4 Bounds on anomalous $\gamma\gamma H$ and $Z\gamma H$ couplings

In this section we develop a strategy to work out the sensitivity of the process  $e\gamma \rightarrow eH$  to the anomalous couplings  $d_{\gamma\gamma}$ ,  $d_{\gamma Z}$  and  $\bar{d}_{\gamma\gamma}$ ,  $\bar{d}_{\gamma Z}$  introduced by the effective lagrangian defined in the previous section. The ability to distinguish an anomalous signal will depend on the relative importance of the deviation in the  $e\gamma \rightarrow eH$  cross section  $\sigma_S(\kappa)$ , where

$$\kappa = d_{\gamma\gamma}, d_{\gamma Z}, \bar{d}_{\gamma\gamma}, \bar{d}_{\gamma Z}, \quad (7)$$

over the SM background. The latter will be made up of both the SM  $e\gamma \rightarrow eH$  cross section  $\sigma_S(0)$  and all the relevant backgrounds  $\sigma_B$  to the  $e\gamma \rightarrow eH \rightarrow ebb\bar{b}$  signal. As discussed in Section 2,  $\sigma_B$  is given by the processes  $e\gamma \rightarrow ebb\bar{b}$  and  $e\gamma \rightarrow e c\bar{c}$  (reducing the  $e\gamma \rightarrow e c\bar{c}$  cross section by a factor 1/10 in order to take into account a 10% probability of misidentifying a  $c$  quark into a  $b$  quark). In this comparison, the available total integrated luminosity  $\mathcal{L}_{int}$  is of course a crucial parameter. In particular, we compare the excess in the number of observed events due to anomalous couplings

$$N^{\text{anom}}(\kappa) = \mathcal{L}_{int} \cdot [\sigma_S(\kappa) - \sigma_S(0)] \quad (8)$$

with the total number of observed events

$$N^{\text{tot}}(\kappa) = \mathcal{L}_{int} \cdot [\sigma_S(\kappa) + \sigma_B]. \quad (9)$$

Then, the requirement that no deviation from the SM cross section is observed at the 95% CL reads:

$$N^{\text{anom}}(\kappa) < 1.96 \cdot \sqrt{N^{\text{tot}}(\kappa)}. \quad (10)$$

In the following, we assume  $m_H = 120$  GeV and make the analysis at two different c.m. collision energies, i.e.  $\sqrt{s} = 500$  GeV and 1.5 TeV, with integrated luminosity  $\mathcal{L}_{int} = 10^2$  and  $10^3$  fb $^{-1}$ , respectively. Correspondingly, the cross sections  $\sigma_S(\kappa)$  and  $\sigma_B$  will be subjected to two different sets of kinematical cuts, optimizing the  $S/B$  ratio according to the c.m. collision energy :

- a) at  $\sqrt{s} = 500$  GeV, we require  $\theta_{b(c)-beam} > 18^\circ$
- b) at  $\sqrt{s} = 1500$  GeV, we require  $\theta_{b(c)-beam} > 8^\circ$

$(P_e, p_T^e)$	(0,0)	(0,100)	(1,0)	(1,100)	(-1,0)	(-1,100)
$\sigma_B$	7.69	0.432	6.39	0.230	9.02	0.632
$\sigma_S(0)$	3.26	0.370	2.66	0.0264	3.86	0.718
$C_1 \times 10^{-2}$	-14.7	-1.55	-12.8	-0.462	-16.4	-2.66
$C_2 \times 10^{-1}$	-8.47	-5.94	4.17	1.79	-21.1	-13.6
$C_3$	-4.50	-2.30	0.50	-0.30	-1.0	-5.50
$C_4$	-2.25	-1.32	-0.450	-0.175	-3.95	-2.85
$C_5 \times 10^{-4}$	17.8	2.57	17.7	2.58	17.7	2.57
$C_6 \times 10^{-3}$	8.49	5.96	6.84	4.74	10.2	7.03
$C_7 \times 10^{-4}$	17.7	2.58	17.8	2.58	17.7	2.57
$C_8 \times 10^{-3}$	8.62	5.95	6.93	4.76	10.1	7.06
$C_9 \times 10^{-3}$	3.73	2.48	-34.5	-21.9	42.3	27.0
$C_{10} \times 10^{-3}$	3.81	2.52	-35.9	-21.8	41.9	26.9

Table 1:  $\sigma_B$ ,  $\sigma_S(0)$  and  $C_i$  coefficients (in fb) for  $\sqrt{S} = 500$  GeV, e-beam polarizations  $P_e = 0, 1, -1$  and final electron transverse momentum cuts  $p_T^e > 0$  and  $p_T^e > 100$  GeV (a cut on the final electron angle  $\theta_e < 90^\circ$  is applied for  $p_T^e > 100$  GeV).

where  $\theta_{b(c)-beam}$  stands for the angle that each final  $b(c)$  quark forms with either of the initial beams. These cuts strongly deplete the  $e\gamma \rightarrow eb\bar{b}$  and  $e\gamma \rightarrow ec\bar{c}$  backgrounds. Also, we integrate the invariant mass distribution of the  $b(c)$  pairs only on the interval  $\pm\Delta m_{b\bar{b}(c\bar{c})} = \pm 3$  GeV around  $m_H$ , in order to keep only that fraction of the background that can fake the Higgs boson decay within the experimental resolution.

Furthermore, in order to enhance either the  $d_{\gamma\gamma}$  or the  $d_{\gamma Z}$  vertex sensitivity, we either integrate over the complete final electron transverse momentum  $p_T^e$  or put a minimum cut  $p_T^e > 100$  GeV.

At  $\sqrt{s} = 500$  GeV, in the  $p_T^e > 100$  GeV case we apply a further cut  $\theta_e < 90^\circ$ , that is we select only the events with a forward final electrons. In this way, we exploit the stronger electron asymmetry in the  $e\gamma \rightarrow eH$  process (both in its SM and its anomalous components) with respect to the  $e\gamma \rightarrow eb\bar{b}$  and  $e\gamma \rightarrow ec\bar{c}$  backgrounds. At larger  $\sqrt{s}$  this difference tends to fade away.

After applying all the cuts described above, the cross section  $\sigma_S(\kappa)$  can be parameterized as a quadratic form in the couplings  $\kappa$

$$\begin{aligned}
\sigma_S(\kappa) &= \sigma_S(0) + d_{\gamma\gamma}C_1 + d_{\gamma Z}C_2 + \bar{d}_{\gamma\gamma}C_3 + \bar{d}_{\gamma Z}C_4 + d_{\gamma\gamma}^2C_5 + d_{\gamma Z}^2C_6 + \bar{d}_{\gamma\gamma}^2C_7 + \bar{d}_{\gamma Z}^2C_8 \\
&+ d_{\gamma\gamma}d_{\gamma Z}C_9 + \bar{d}_{\gamma\gamma}\bar{d}_{\gamma Z}C_{10}
\end{aligned} \tag{11}$$

where the numerical coefficients for  $\sigma_S(0)$  and  $C_i$  for  $m_H = 120$  GeV are given in tables 1 and 2 for  $\sqrt{S} = 500$  GeV and  $\sqrt{S} = 1500$  GeV, respectively. The corresponding values of  $\sigma_B$  are



$(P_e, p_T^e)$	(0,0)	(0,100)	(1,0)	(1,100)	(-1,0)	(-1,100)
$\sigma_B$	2.48	0.398	2.18	0.210	2.78	0.586
$\sigma_S(0)$	1.57	0.437	1.05	0.0262	2.11	0.838
$C_1 \times 10^{-2}$	-7.44	-2.25	-5.29	-0.454	-9.57	-4.04
$C_2 \times 10^{-2}$	-1.12	-1.02	0.280	0.175	-2.55	-2.23
$C_3$	0	0.20	-4.50	0.150	-3.50	-0.650
$C_4$	-0.60	-0.70	-0.150	-0.150	-0.650	-0.60
$C_5 \times 10^{-4}$	12.2	5.79	12.2	5.79	12.2	5.83
$C_6 \times 10^{-4}$	1.92	1.68	1.53	1.34	2.31	2.03
$C_7 \times 10^{-4}$	12.2	5.77	12.2	5.80	12.2	5.80
$C_8 \times 10^{-4}$	1.94	1.68	1.54	1.34	2.28	2.02
$C_9 \times 10^{-4}$	0.739	0.663	-6.51	-5.53	8.05	6.79
$C_{10} \times 10^{-4}$	0.741	0.639	-6.43	-5.48	7.90	6.84

Table 2: The same results as in table 1, but for  $\sqrt{S} = 1500$  GeV (with no restriction on the final electron angle for  $p_T^e > 100$  GeV).

also shown. With the help of the above parameterization and according to the definition of  $N^{\text{anom}}(\kappa)$  and  $N^{\text{tot}}(\kappa)$  given above, one can then develop all the numerical analysis that we are going to present in the next section.

## 5 Numerical results

We now present the results of our analysis. In figs. 1-16, for two values of  $\sqrt{s}$  (500 and 1500 GeV), and of the minimum cut on  $p_T^e$  (0 and 100 GeV), we show the contour plots that select the area that satisfies the condition in eq.(10), in the planes of some interesting combination of pairs of couplings [i.e.,  $(d_{\gamma\gamma}, d_{\gamma Z}), (d_{\gamma\gamma}, \bar{d}_{\gamma\gamma}), (d_{\gamma Z}, \bar{d}_{\gamma Z}), (\bar{d}_{\gamma\gamma}, \bar{d}_{\gamma Z})$ ]. All the couplings different from the ones on the  $(x, y)$  axis are assumed to be zero. The solid, dot-dashed, dashed (generally closed) lines refer to the values  $P_e = 0, -1, +1$  for the polarization of the  $e$  beam, respectively. The darker curve among the three (or two) curves for each case corresponds to the set of points where the cross section gets its SM value, that is the set of solutions  $\kappa_{SM}$  of the equation

$$\sigma_S(\kappa_{SM}) = \sigma_S(0) \rightarrow N^{\text{anom}}(\kappa_{SM}) = 0. \quad (12)$$

We call these curves *SM curves*. The lighter curves instead correspond to the equality condition of the two members in eq.(10). Hence, in general, by requiring that no deviation from the SM rates is observed at the 95% CL, we will be able to exclude all the parameters plane but the area between the two lighter curves. Note that in some cases the internal, lighter curve is not shown (see figs. 3-8, 11-16). Indeed, in these cases the equality in eq.(10) has just one curve

as solution. In the latter cases one will be able to exclude all the parameter plane but the area inside the unique light curve, that of course contains the *SMcurve*.

Note also that in many cases we magnified the axis scale in order to better distinguish the details of the smaller curves, loosing in such a way some portion of the more extended contours, that are, however, less relevant in order to set the best limits on the anomalous couplings.

In general, the two 95% CL curves define a *strip* in the plane, some portion of which is quite far from the point (0,0), the point where any non-excluded region should be naturally centered around. These “far-away” portions can be removed by combining the data relative to different polarizations of the electron beam and/or different sets of kinematical cuts. For instance, in figure 1, in the plane  $(d_{\gamma\gamma}, d_{\gamma Z})$ , by comparing the bounds corresponding to the  $P_e = 0, -1, +1$  polarization at  $\sqrt{s} = 500$  GeV and  $p_T^e > 0$ , one can exclude most of the area far from the  $(d_{\gamma\gamma} = 0, d_{\gamma Z} = 0)$  point. The remaining three intersection regions which are far from the origin can be removed by adding the information from figure 5. Here, the same case of figure 1 is studied with an additional cut  $p_T^e > 100$  GeV (and  $\theta_e < 90^\circ$ ), and one is left with just two intersection regions. Combining the informations in both figures, the only surviving area is the one around (0, 0). The extension of this area is of course strictly connected to the sensibility of the  $e\gamma \rightarrow eH$  process to the  $d_{\gamma\gamma}$  and  $d_{\gamma Z}$  couplings.

Note that, because of the interference effects with the SM cross section, the plots are in general asymmetric with respect to the zero of the  $d_{\gamma\gamma}$  and  $d_{\gamma Z}$  couplings. On the other hand, the CP-odd variables  $\bar{d}_{\gamma\gamma}$  and  $\bar{d}_{\gamma Z}$  shows modest interference effects, as discussed in Section 3.

In order to make a more quantitative discussion, it is useful to go through the corresponding one-dimensional limits on the anomalous couplings.

In tables 3-6 we show the 95% CL limits on each anomalous coupling (according to eq.(10)), when the remaining three couplings are switched off. Tables 3-4 are relative to the  $\sqrt{s} = 500$  GeV,  $\mathcal{L}_{int} = 10^2 \text{fb}^{-1}$  case, while tables 5-6 refer to  $\sqrt{s} = 1500$  GeV,  $\mathcal{L}_{int} = 10^3 \text{fb}^{-1}$ . We assume  $m_H = 120$  GeV and the kinematical cuts are the same as described above for the corresponding cases in figure 1-16.

In each case, we first show the bounds on the  $\gamma\gamma H$  vertex couplings  $(d_{\gamma\gamma}, \bar{d}_{\gamma\gamma})$  and on the  $Z\gamma H$  vertex couplings  $(d_{\gamma Z}, \bar{d}_{\gamma Z})$  (cf. tables 3 and 5). Then we present the corresponding bounds on the anomalous couplings that are directly associated to the operators of the effective lagrangian,  $d, d_B, \bar{d}, \bar{d}_B$  (cf. tables 4 and 6). In each table, three fixed polarization state ( $P_e = 0, -1, +1$ ) for the electron beam and two different choices for the  $p_T^e$  cut are presented.

In general the limits on the different parameters range in the interval

$$|\kappa| < 10^{-4} - 10^{-2}, \quad (13)$$

also depending on the c.m. energy. One can see that the choice  $p_T^e > 100$  GeV improves the limits on the  $d_{\gamma Z}$  and  $\bar{d}_{\gamma Z}$  parameters with respect to the  $p_T^e > 0$  case. The opposite is true for the  $d_{\gamma\gamma}$  and  $\bar{d}_{\gamma\gamma}$  couplings, since the  $\gamma\gamma H$  vertex mostly contribute to the low- $p_T^e$  cross section.

The effect of the  $e$ -beam polarization is different for different parameters. At  $\sqrt{s} = 500$  GeV, the  $P_e = -1$  polarization improves the limits on the  $d_{\gamma\gamma}$  and  $d_{\gamma z}$  couplings, especially at large values of  $p_T^e$ . On the other hand, the bounds on the CP violating couplings gets weaker with respect to the unpolarized case. The opposite happens for the  $P_e = 1$  polarization.

Referring to the  $d, d_B, \bar{d}$  and  $\bar{d}_B$  set of bounds, considerably better limits are obtained for the couplings  $d_B$  and  $\bar{d}_B$ , which enter with a coefficient  $(\tan\theta_W)^{-1} \sim 1.8$  in the combinations giving  $d_{\gamma\gamma}$  and  $\bar{d}_{\gamma\gamma}$  in eq.(6).

Concerning the polarization effects,  $P_e = 1$  improves the limits on  $d_B$  and  $\bar{d}_B$  especially at large  $p_T^e$ . On the other hand,  $P_e = -1$  improves the  $d, d_B$ , and  $\bar{d}$  cases, while worsens the  $\bar{d}_B$  case.

A similar discussion applies to the  $\sqrt{s} = 1.5$  TeV case. Note that the clear improvement in the set of the coupling bounds with respect to the lower c.m energy case is only slightly due to the different value of  $\sqrt{s}$ . The crucial effect comes from the factor 10 of increase in the assumed integrated luminosity at  $\sqrt{s} = 1.5$  TeV.

From the results presented in tables 3-6 we draw the following conclusions:

- The strongest bounds on the CP-even  $d_{\gamma\gamma}$  and CP-odd  $\bar{d}_{\gamma\gamma}$  couplings are at the level of  $|d_{\gamma\gamma}| \lesssim 5 \times 10^{-4}$ ,  $|\bar{d}_{\gamma\gamma}| \lesssim 2 \times 10^{-3}$  at  $\sqrt{s} = 500$  GeV, and  $|d_{\gamma\gamma}| \lesssim 2 \times 10^{-4}$ ,  $|\bar{d}_{\gamma\gamma}| \lesssim 1 \times 10^{-3}$  at  $\sqrt{s} = 1500$  GeV. They are obtained in the case when no cut on  $p_T^e$  is imposed. In both the CP-even and CP-odd cases these bounds are only slightly sensitive to the initial  $e$ -beam polarization.
- The strongest limits on the CP-even coupling  $d_{\gamma z}$  are at the level of  $|d_{\gamma z}| \lesssim 2 \times 10^{-3}$  at  $\sqrt{s} = 500$  GeV, and  $|d_{\gamma z}| \lesssim 3 \times 10^{-4}$  at  $\sqrt{s} = 1500$  GeV, and are obtained from a left-handed polarized electron beam ( $P_e = -1$ ) by imposing a  $p_T^e > 100$  GeV cut. On the other hand, in the CP-odd case, the right-handed polarized electron beam ( $P_e = 1$ ) gives the best performance, with bounds at the level of  $|\bar{d}_{\gamma z}| \lesssim 5 \times 10^{-3}$  at  $\sqrt{s} = 500$  GeV, and  $|\bar{d}_{\gamma z}| \lesssim 1.5 \times 10^{-3}$  at  $\sqrt{s} = 1500$  GeV. Indeed, in the latter case, the violation of the strong destructive interference between the  $\gamma\gamma H$  and  $Z\gamma H$  terms by the anomalous terms compensates the decrease in statistics.

The analogous results for the bounds on the CP-even  $d, d_B$  and CP-odd  $\bar{d}, \bar{d}_B$  anomalous couplings (see eq. (6)) can be outlined as follows:

- The strongest bounds on the CP-even couplings at  $\sqrt{s} = 500$  GeV are at the level of  $|d| \lesssim 6 \times 10^{-4}$ , obtained at  $P_e = -1$ , and  $|d_B| \lesssim 2.5 \times 10^{-4}$  (with no cut on  $p_T^e$ ), not depending on the  $e$  polarization. At  $\sqrt{s} = 1500$  GeV, one has  $|d| \lesssim 1.7 \times 10^{-4}$ , obtained at  $P_e = -1$  and  $p_T^e > 100$  GeV, and  $|d_B| \lesssim 1 \times 10^{-4}$  (with no cut on  $p_T^e$ ), not depending on the  $e$  polarization.
- The strongest bounds on the CP-odd couplings at  $\sqrt{s} = 500$  GeV are  $|\bar{d}| \lesssim 3 \times 10^{-3}$  and  $|\bar{d}_B| \lesssim 1 \times 10^{-3}$ , which are obtained for  $P_e = -1$  and  $P_e = 1$ , respectively. These bounds

are quite insensitive to the cuts on  $p_T^e$ . At  $\sqrt{s} = 1500$  GeV, one has  $|\bar{d}| \lesssim 1.0 \times 10^{-3}$  for  $P_e = -1$ , with  $p_T^e > 100$  GeV, and  $|\bar{d}_B| \lesssim 3 \times 10^{-4}$ , for  $P_e = 1$ , with  $p_T^e > 100$  GeV.

Other processes have been studied in the literature that could be able to bound the parameters  $d$ ,  $d_B$ ,  $\bar{d}$ ,  $\bar{d}_B$  at future linear colliders. In particular, the processes  $e^+e^- \rightarrow HZ$  and  $\gamma\gamma \rightarrow H$  have been studied for a  $e^+e^-$  collider at  $\sqrt{s} = 1$  TeV and with  $80 \text{ fb}^{-1}$  by Gounaris et al. From  $e^+e^- \rightarrow HZ$ , they get  $|d| \lesssim 5 \times 10^{-3}$ ,  $|d_B| \lesssim 2.5 \times 10^{-3}$ ,  $|\bar{d}| \lesssim 5 \times 10^{-3}$  and  $|\bar{d}_B| \lesssim 2.5 \times 10^{-3}$  [15]. The process  $\gamma\gamma \rightarrow H$  can do a bit better and reach the values  $|d| \lesssim 1 \times 10^{-3}$ ,  $|d_B| \lesssim 3 \times 10^{-4}$ ,  $|\bar{d}| \lesssim 4 \times 10^{-3}$  and  $|\bar{d}_B| \lesssim 1.3 \times 10^{-3}$ , assuming a particular photon energy spectrum [16]. These analysis assume a precision of the measured production rate equal to  $1/\sqrt{N}$  (with  $N$  the total number of events), and neglect possible backgrounds. In order to set the comparative potential of our process with respect to these two processes in bounding the parameters  $d$ ,  $d_B$ ,  $\bar{d}$ ,  $\bar{d}_B$ , according to the discussion at the end of section 1, we assumed  $\sqrt{s} = 0.9$  TeV and (conservatively) a luminosity of  $25 \text{ fb}^{-1}$  in  $e\gamma \rightarrow eH$ . We then neglected any background, and assumed a precision equal to  $1/\sqrt{N}$ . In the case  $P_e = 0$  and  $p_T^e > 0$ , we get  $|d| \lesssim 5 \times 10^{-4}$ ,  $|d_B| \lesssim 2 \times 10^{-4}$ ,  $|\bar{d}| \lesssim 2 \times 10^{-3}$  and  $|\bar{d}_B| \lesssim 8 \times 10^{-4}$ . This analysis confirms the excellent potential of the process  $e\gamma \rightarrow eH$ . Note however that the  $\gamma\gamma \rightarrow H$  process has the further advantage of isolating the  $d_{\gamma\gamma}$  anomalous component from a possible non-zero  $d_{\gamma Z}$  contribution [11], contrary to the channel  $e\gamma \rightarrow eH$ , where the effects of the two couplings are superimposed.

## 6 Conclusions

We performed a complete study of the potential of the process  $e\gamma \rightarrow eH$  for discovering possible  $\gamma\gamma H$  and  $Z\gamma H$  anomalous couplings. In the effective lagrangian formalism, we concentrated on the  $dim = 6$  operators that can not be constrained through the process  $e^+e^- \rightarrow WW$ . We included a detailed analysis of all the relevant backgrounds and the possibility of longitudinal polarization for the electron beam. We also studied the set of kinematical cuts that optimizes the signal to background ratio. We found that the  $e\gamma \rightarrow eH$  gives the possibility to improve considerably the constrains on the  $d$ ,  $d_B$ ,  $\bar{d}$ ,  $\bar{d}_B$  couplings that can be obtained by other processes. Following the conventions of [17], one can convert these constrains into upper limits of the NP scale  $\Lambda$  that can be explored through  $e\gamma \rightarrow eH$  with  $\sqrt{s} \simeq 1.5$  TeV and  $10^3 \text{ fb}^{-1}$ :

$$\begin{aligned}
|d| \lesssim 1.7 \times 10^{-4} &\rightarrow \left| \frac{f_{WW}}{\Lambda^2} \right| \lesssim 0.026 \text{ TeV}^{-2} \\
|d_B| \lesssim 1 \times 10^{-4} &\rightarrow \left| \frac{f_{BB}}{\Lambda^2} \right| \lesssim 0.015 \text{ TeV}^{-2} \\
|\bar{d}| \lesssim 1 \times 10^{-3} &\rightarrow \left| \frac{\bar{f}_{WW}}{\Lambda^2} \right| \lesssim 0.15 \text{ TeV}^{-2} \\
|\bar{d}_B| \lesssim 3 \times 10^{-4} &\rightarrow \left| \frac{\bar{f}_{WW}}{\Lambda^2} \right| \lesssim 0.046 \text{ TeV}^{-2}
\end{aligned} \tag{14}$$

$P_e = 0$	$p_T^e > 0$	$p_T^e > 100 \text{ GeV}$
$d_{\gamma\gamma} \times 10^3$	(-0.44, 0.46)	(-1.1, 1.3)
$d_{\gamma Z} \times 10^3$	(-5.3, 15)	(-2.7, 5.0)
$\bar{d}_{\gamma\gamma} \times 10^3$	(-2.0, 2.0)	(-2.7, 2.8)
$\bar{d}_{\gamma Z} \times 10^3$	(-8.8, 9.0)	(-5.7, 5.9)
$P_e = 1$	$p_T^e > 0$	$p_T^e > 100 \text{ GeV}$
$d_{\gamma\gamma} \times 10^3$	(-0.46, 0.49)	(-1.5, 3.3)
$d_{\gamma Z} \times 10^3$	(-13, 7.0)	(-7.3, 3.5)
$\bar{d}_{\gamma\gamma} \times 10^3$	(-1.9, 1.9)	(-2.2, 2.2)
$\bar{d}_{\gamma Z} \times 10^3$	(-9.4, 9.5)	(-5.1, 5.1)
$P_e = -1$	$p_T^e > 0$	$p_T^e > 100 \text{ GeV}$
$d_{\gamma\gamma} \times 10^3$	(-0.43, 0.45)	(-0.88, 0.88)
$d_{\gamma Z} \times 10^3$	(-3.1, 4.1)	(-1.7, 1.7)
$\bar{d}_{\gamma\gamma} \times 10^3$	(-2.0, 2.0)	(-2.9, 3.1)
$\bar{d}_{\gamma Z} \times 10^3$	(-10, 11)	(-6.5, 6.9)

Table 3: Bounds on the CP-even  $d_{\gamma\gamma}$ ,  $d_{\gamma Z}$  and CP-odd  $\bar{d}_{\gamma\gamma}$ ,  $\bar{d}_{\gamma Z}$  anomalous couplings, for  $\sqrt{S} = 500 \text{ GeV}$ ,  $e$ -beam polarizations  $P_e = 0, 1, -1$ , and for  $p_T^e > 0$  and  $p_T^e > 100 \text{ GeV}$ . In the case  $p_T^e > 100 \text{ GeV}$ , a cut on the final electron angle  $\theta_e < 90^\circ$  is applied (see text).

For  $f_i \sim 1$  one can explore energy scales up to about 6, 8, 2.6 and about 4.5 TeV, respectively. At  $\sqrt{s} \simeq 500 \text{ GeV}$  and  $10^2 \text{ fb}^{-1}$ , the corresponding constraints on the couplings are a factor 2 or 3 weaker than above (reflecting into energy scales  $\Lambda$  lower by a factor 1.4 or 1.7, respectively), mainly because of the smaller integrated luminosity assumed.

## Acknowledgements

E.G. would like to thank C. Di Cairano and A.M. Turiel for useful discussions. E.G. acknowledges the financial support of the TMR network project ref. FMRX-CT96-0090 and partial financial support from the CICYT project ref. AEN97-1678. V.I. acknowledges the financial support of the Grant Center of the St.Petersburg St. University.

$P_e = 0$	$p_T^e > 0$	$p_T^e > 100 \text{ GeV}$
$d \times 10^3$	(-0.73, 0.76)	(-1.2, 1.3)
$d_B \times 10^3$	(-0.25, 0.26)	(-0.70, 3.3)
$\bar{d} \times 10^3$	(-3.2, 3.3)	(-3.6, 3.7)
$\bar{d}_B \times 10^3$	(-1.1, 1.1)	(-1.5, 1.5)
$P_e = 1$	$p_T^e > 0$	$p_T^e > 100 \text{ GeV}$
$d \times 10^3$	(-0.89, 0.94)	(-10, 25)
$d_B \times 10^3$	(-0.24, 0.26)	(-0.65, 1.4)
$\bar{d} \times 10^3$	(-3.9, 3.9)	(-15, 15)
$\bar{d}_B \times 10^3$	(-0.97, 0.96)	(-0.97, 0.97)
$P_e = -1$	$p_T^e > 0$	$p_T^e > 100 \text{ GeV}$
$d \times 10^3$	(-0.63, 0.66)	(-0.83, 0.83)
$d_B \times 10^3$	(-0.25, 0.26)	(-0.67, 0.66)
$\bar{d} \times 10^3$	(-3.1, 3.2)	(-2.9, 3.1)
$\bar{d}_B \times 10^3$	(-1.2, 1.2)	(-2.3, 2.4)

Table 4: Bounds on the CP-even  $d$ ,  $d_B$  and CP-odd  $\bar{d}$ ,  $\bar{d}_B$  anomalous couplings, for  $\sqrt{S} = 500 \text{ GeV}$ ,  $e$ -beam polarizations  $P_e = 0, 1, -1$ , and for  $p_T^e > 0$  and  $p_T^e > 100 \text{ GeV}$ . In the case  $p_T^e > 100 \text{ GeV}$ , a cut on the final electron angle  $\theta_e < 90^\circ$  is applied (see text).

$P_e = 0$	$p_T^e > 0$	$p_T^e > 100 \text{ GeV}$
$d_{\gamma\gamma} \times 10^3$	(-0.17, 0.17)	(-0.25, 0.26)
$d_{\gamma Z} \times 10^3$	(-0.98, 1.5)	(-0.51, 0.58)
$\bar{d}_{\gamma\gamma} \times 10^3$	(-1.0, 1.0)	(-0.96, 0.98)
$\bar{d}_{\gamma Z} \times 10^3$	(-2.6, 2.6)	(-1.8, 1.8)
$P_e = 1$	$p_T^e > 0$	$p_T^e > 100 \text{ GeV}$
$d_{\gamma\gamma} \times 10^3$	(-0.21, 0.22)	(-0.44, 1.2)
$d_{\gamma Z} \times 10^3$	(-3.8, 2.0)	(-2.1, 1.0)
$\bar{d}_{\gamma\gamma} \times 10^3$	(-0.96, 0.99)	(-0.73, 0.71)
$\bar{d}_{\gamma Z} \times 10^3$	(-2.7, 2.7)	(-1.5, 1.5)
$P_e = -1$	$p_T^e > 0$	$p_T^e > 100 \text{ GeV}$
$d_{\gamma\gamma} \times 10^3$	(-0.15, 0.15)	(-0.18, 0.18)
$d_{\gamma Z} \times 10^3$	(-0.53, 0.57)	(-0.33, 0.33)
$\bar{d}_{\gamma\gamma} \times 10^3$	(-1.1, 1.1)	(-1.1, 1.1)
$\bar{d}_{\gamma Z} \times 10^3$	(-2.6, 2.6)	(-1.9, 1.9)

Table 5: Bounds on the CP-even  $d_{\gamma\gamma}$ ,  $d_{\gamma Z}$  and CP-odd  $\bar{d}_{\gamma\gamma}$ ,  $\bar{d}_{\gamma Z}$  anomalous couplings, for  $\sqrt{S} = 1.5\text{TeV}$ ,  $e$ -beam polarizations  $P_e = 0, 1, -1$ , and for  $p_T^e > 0$  and  $p_T^e > 100 \text{ GeV}$  (no restriction on the final electron angle).

$P_e = 0$	$p_T^e > 0$	$p_T^e > 100 \text{ GeV}$
$d \times 10^3$	(-0.24, 0.25)	(-0.25, 0.25)
$d_B \times 10^3$	(-0.10, 0.10)	(-0.17, 0.21)
$\bar{d} \times 10^3$	(-1.5, 1.5)	(-1.2, 1.2)
$\bar{d}_B \times 10^3$	(-5.6, 5.6)	(-0.52, 0.53)
$P_e = 1$	$p_T^e > 0$	$p_T^e > 100 \text{ GeV}$
$d \times 10^3$	(-0.4, 0.4)	(-3.3, 17)
$d_B \times 10^3$	(-0.11, 0.12)	(-0.19, 0.49)
$\bar{d} \times 10^3$	(-2.5, 2.7)	(-9.3, 8.1)
$\bar{d}_B \times 10^3$	(-4.5, 4.7)	(-0.31, 0.31)
$P_e = -1$	$p_T^e > 0$	$p_T^e > 100 \text{ GeV}$
$d \times 10^3$	(-0.18, 0.18)	(-0.16, 0.17)
$d_B \times 10^3$	(-0.093, 0.094)	(-0.14, 0.14)
$\bar{d} \times 10^3$	(-1.2, 1.2)	(-0.96, 0.98)
$\bar{d}_B \times 10^3$	(-0.69, 0.71)	(-0.88, 0.90)

Table 6: Bounds on the CP-even  $d$ ,  $d_B$  and CP-odd  $\bar{d}$ ,  $\bar{d}_B$  anomalous couplings, for  $\sqrt{S} = 1500 \text{ GeV}$ ,  $e$ -beam polarizations  $P_e = 0, 1, -1$ , and for  $p_T^e > 0$  and  $p_T^e > 100 \text{ GeV}$  (no restriction on the final electron angle).



## References

- [1] D'Agostini G. and Degrassi G., hep-ph/9902226 and references therein.
- [2] *Physics and Experiments with  $e^+e^-$  Linear Colliders*, ed. Miyamoto A., Fujii Y., Matsui T. and Iwata S., Singapore: World Sci., 1996.
- [3] Proceedings, *Conceptual Design of a 500 GeV  $e^+e^-$  Linear Collider with Integrated X-Ray Laser Facility*, ed. Sjöstrand T. and Zerwas P., DESY 79-048, ECFA-97-181, 1997; Phys. Rep. **C299** (1998) 1.
- [4] Ginzburg I.F. et al., *Nucl.Instr. Methods* **205**, 47 (1983); **219**, 5 (1984); Telnov V.I., *Nucl.Instr. Methods* **A294**, 72 (1990).
- [5] Brinkmann R. et al., *An Interaction Region for  $\gamma\gamma$  and  $e\gamma$  collisions at TESLA/SBLC*, *Nucl. Instrum. Meth.* **A406**, 13 (1998).
- [6] Barroso A., Pulido J., and Romao J.C., *Nucl. Phys.* **B267**, 509 (1985); **B272**, 693 (1986).
- [7] Abbasabadi A. et al., *Phys. Rev.* **D52**, 3919 (1995).
- [8] Djouadi A. et al., *Nucl. Phys.* **B491**, 68 (1997).
- [9] Gabrielli E., Ilyin V.A., and Mele B., *Phys. Rev.* **D56**, 5945 (1997); *erratum-ibid* **D58** 119902 (1998).
- [10] Gabrielli E., Ilyin V.A., and Mele B., in: "Beyond the Standard Model V" (Proc. Fifth Conference, Balholm, Norway April-May 1997), ed. G.Eigen, P.Osland and B.Stugu, AIP, N.-Y., 1997, p.506, hep-ph/9709351; in: Proc. Int. Europhysics Conf on HEP (Jerusalem, Israel, August 1997), ed. D.Lellouch, G.Mikenberg and E.Rabinovoci, Springer, Berlin Heidelberg, 1999, p.1163, hep-ph/9712285.
- [11] Banin A.T., Ginzburg I.F., Ivanov I.P., hep-ph/9806515.
- [12] Baikov P.A. et al., *High Energy Physics and Quantum Field Theory*, ed. Levtchenko B. and Savrin V., Moscow, hep-ph/9701412; Boos E.E et al., SNUTP-94-116, 1994, hep-ph/9503280.
- [13] Cotti U., Diaz-Cruz J.L., Toscano J.J, *Phys. Lett. B* **404**, 308 (1997).
- [14] Buchmüller W., and Wyler D., *Nucl. Phys.* **B268**, 621 (1986).  
Hagiwara K. et al., *Phys. Rev.* **D48**, 2182 (1993); *Phys. Lett.* **B318**, 155 (1993).  
Gounaris G.J. et al., *Nucl. Phys.* **B459**, 51 (1996).
- [15] Hagiwara K. and Stong M.L., *Z. Phys.* **C62** 99 (1994).  
Gounaris G.J., Renard F.M. and Vlachos N.D. *Nucl. Phys.* **B459** 51 (1996).

[16] Gounaris G.J. and Renard F.M., *Z. Phys.* **C69** 513 (1996).

[17] Gounaris G.J. and Renard F.M., hep-ph/9811413.

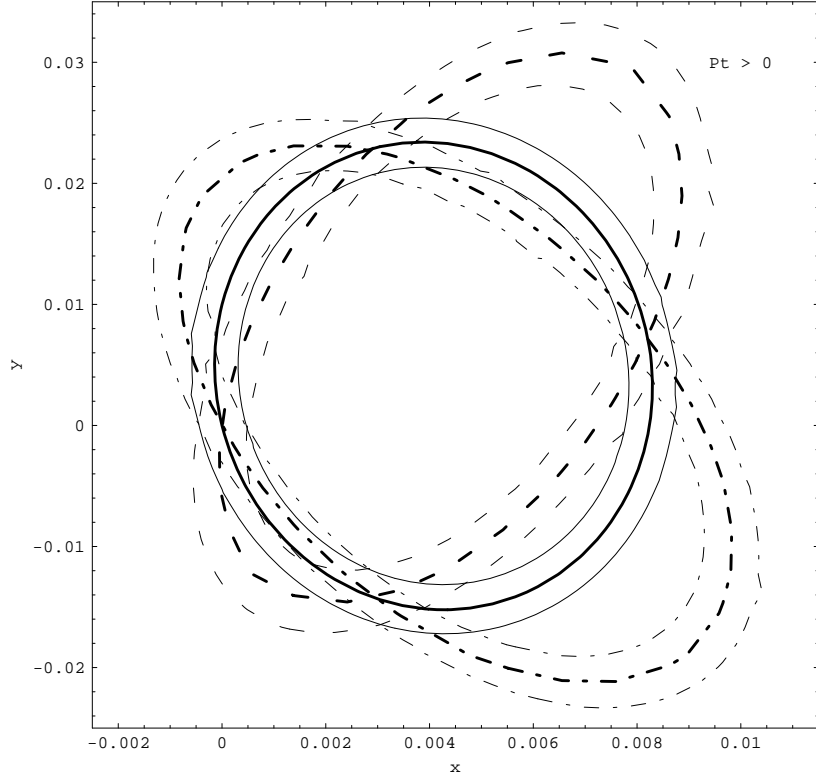


Figure 1: Contour plots for  $\sqrt{S} = 500$  GeV with  $x = d_{\gamma\gamma}$  and  $y = d_{\gamma Z}$  and with a cut  $p_T^e > 0$  (no restriction on the final electron angle  $\theta_e$ ). The continuous, dashed and dashed-dot lines correspond to  $P_e = 0, 1, -1$  e-beam polarization, respectively. The darker curves correspond to the Standard Model solution.

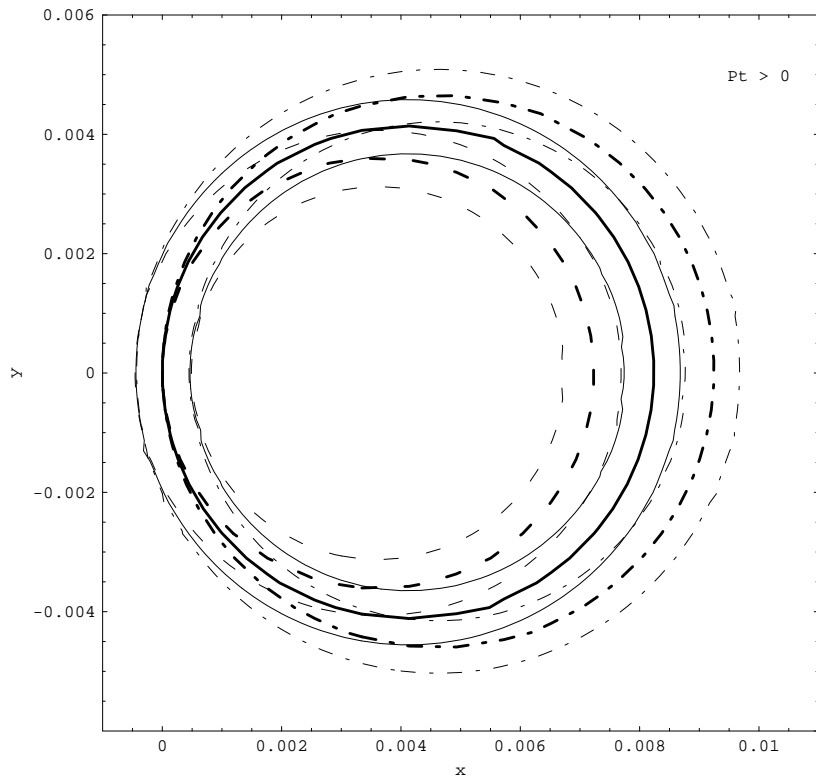


Figure 2: Contour plots as in figure 1 with  $x = d_{\gamma\gamma}$  and  $y = \bar{d}_{\gamma\gamma}$ .

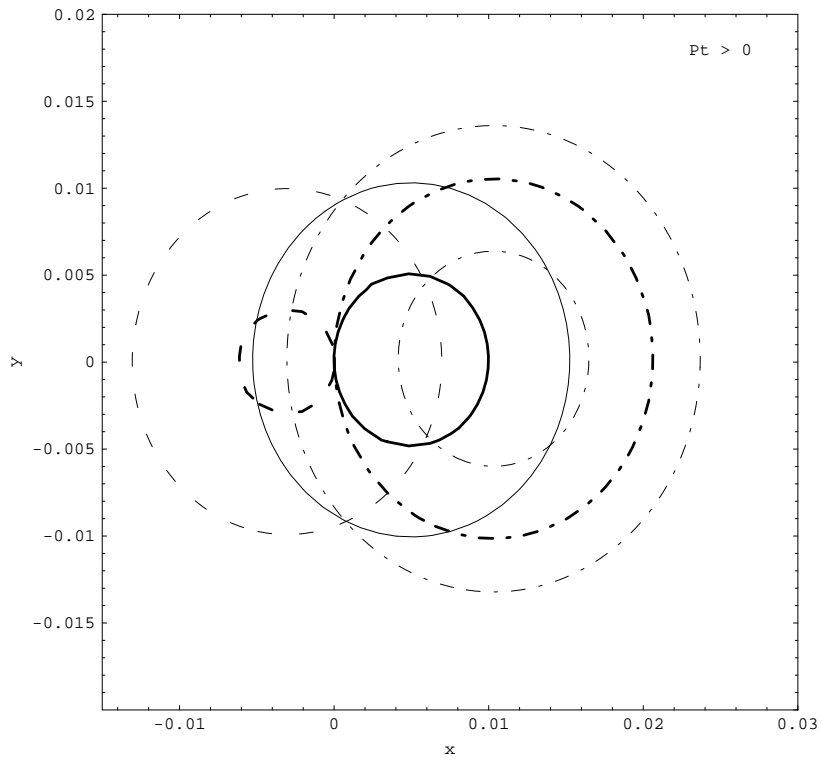


Figure 3: Contour plots as in figure 1 with  $x = d_{\gamma Z}$  and  $y = \bar{d}_{\gamma Z}$ .

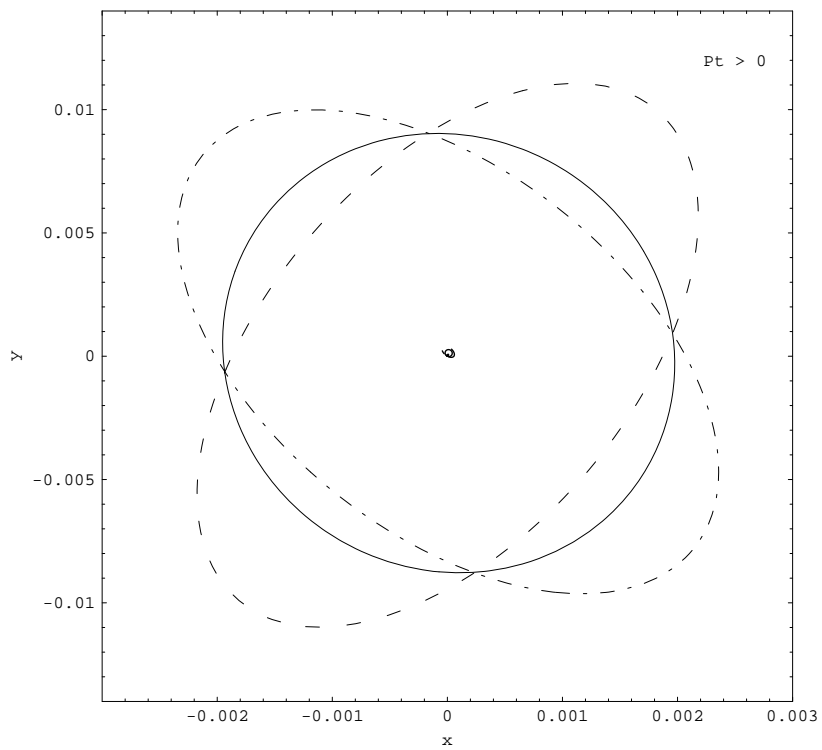


Figure 4: Contour plots as in figure 1 with  $x = \bar{d}_{\gamma\gamma}$  and  $y = \bar{d}_{\gamma Z}$ .

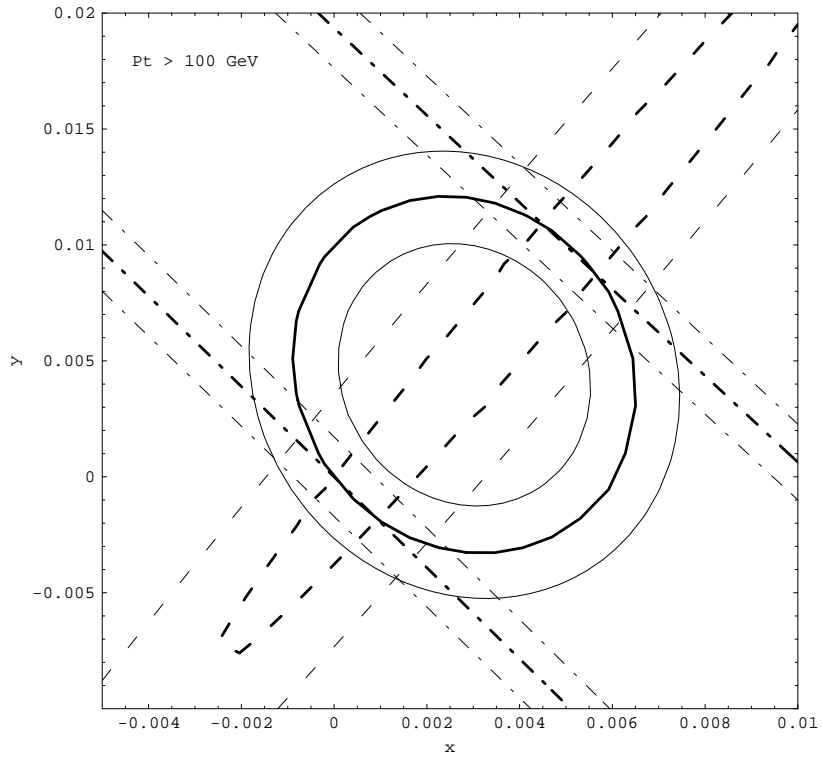


Figure 5: Contour plots as in figure 1 with  $x = d_{\gamma\gamma}$  and  $y = d_{\gamma Z}$ , where the cuts  $p_T^e > 100$  GeV and  $\theta_e < 90^\circ$  on the final electron have been applied.

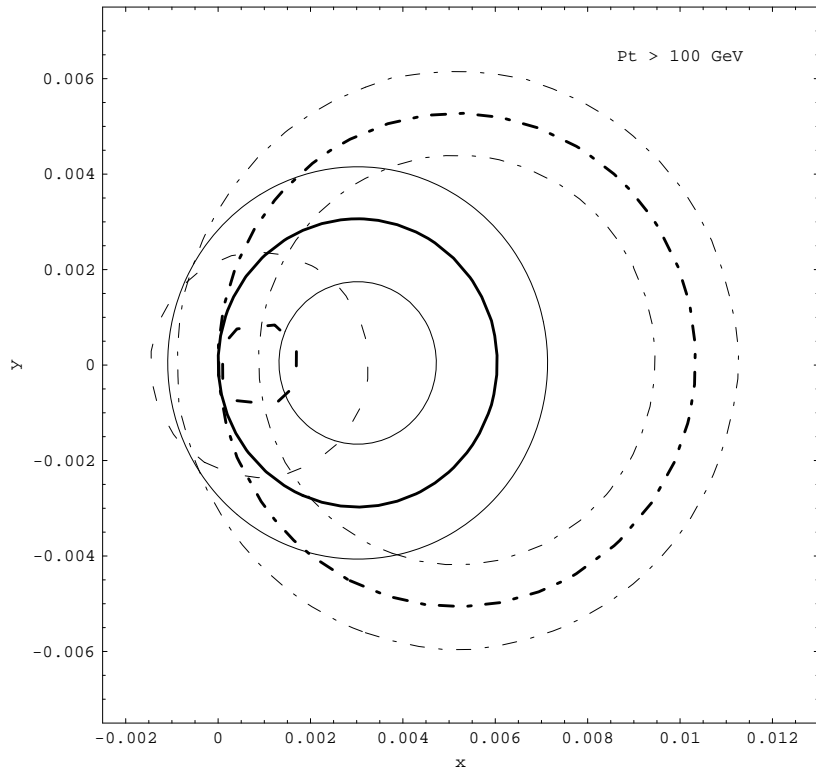


Figure 6: Contour plots as in figure 5 with  $x = d_{\gamma\gamma}$  and  $y = \bar{d}_{\gamma\gamma}$ .



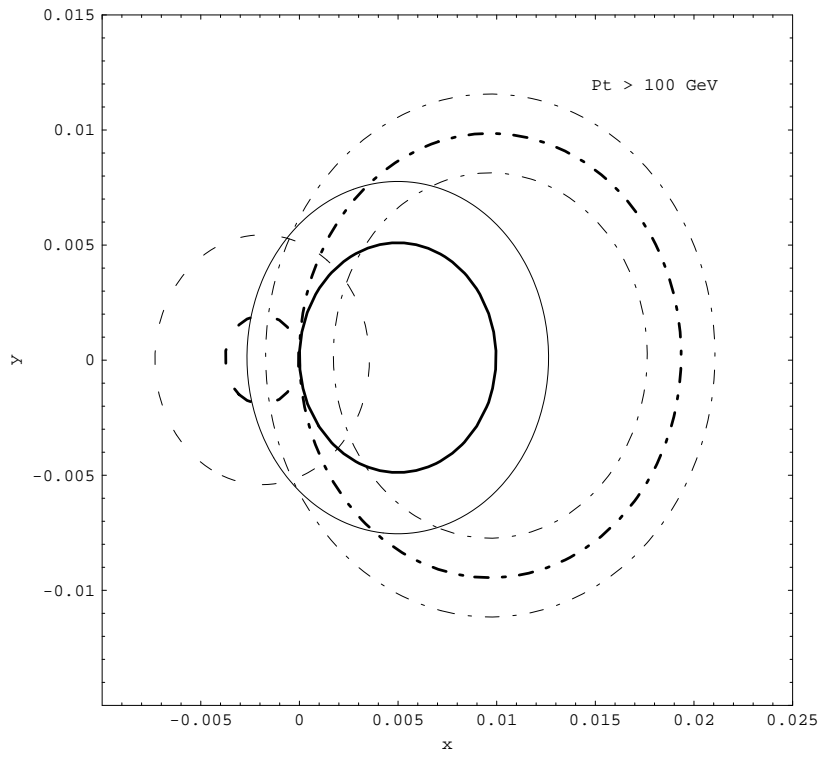


Figure 7: Contour plots as in figure 5 with  $x = d_{\gamma Z}$  and  $y = \bar{d}_{\gamma Z}$ .

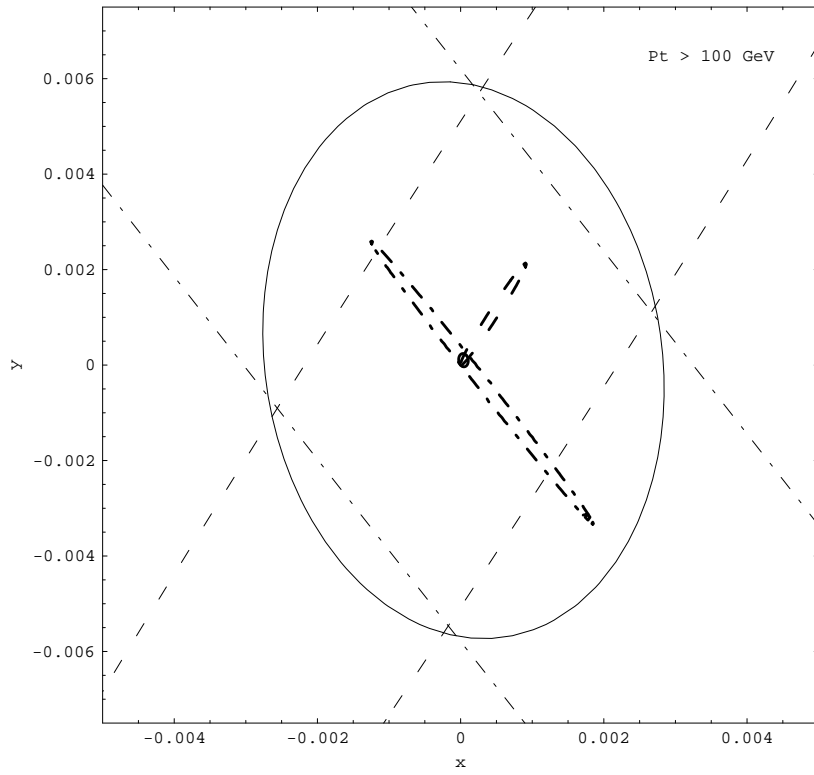


Figure 8: Contour plots as in figure 5 with  $x = \bar{d}_{\gamma\gamma}$  and  $y = \bar{d}_{\gamma Z}$ .

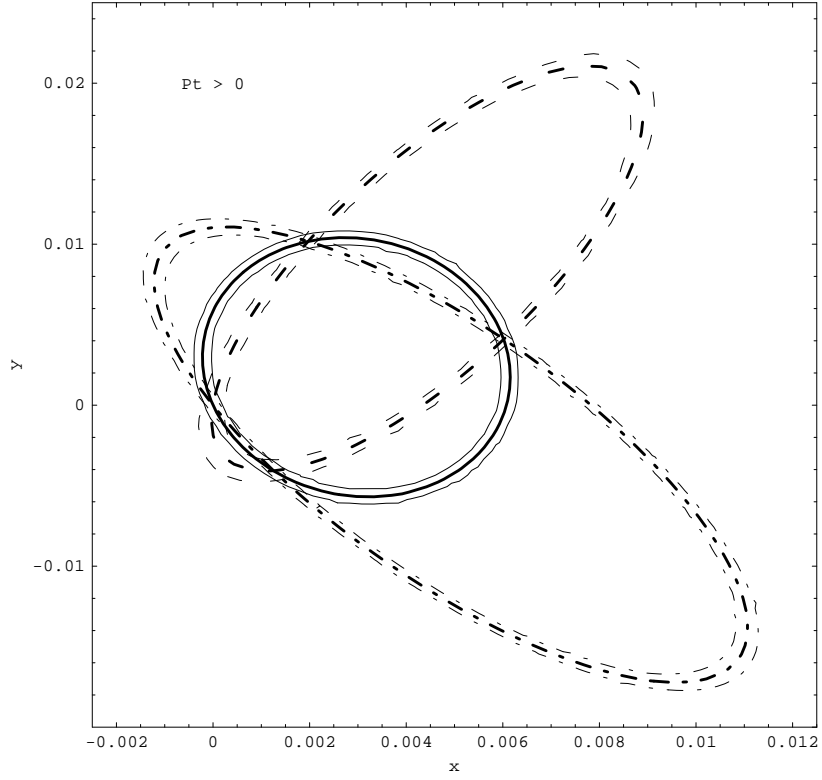


Figure 9: Contour plots for  $\sqrt{S} = 1500$  GeV with  $x = d_{\gamma\gamma}$  and  $y = d_{\gamma Z}$  and with a cut  $p_T^e > 0$  (no restriction on the final electron angle  $\theta_e$ ). The continuous, dashed and dashed-dot lines correspond to  $P_e = 0, 1, -1$  e-beam polarization, respectively. The darker curves correspond to the Standard Model solution.

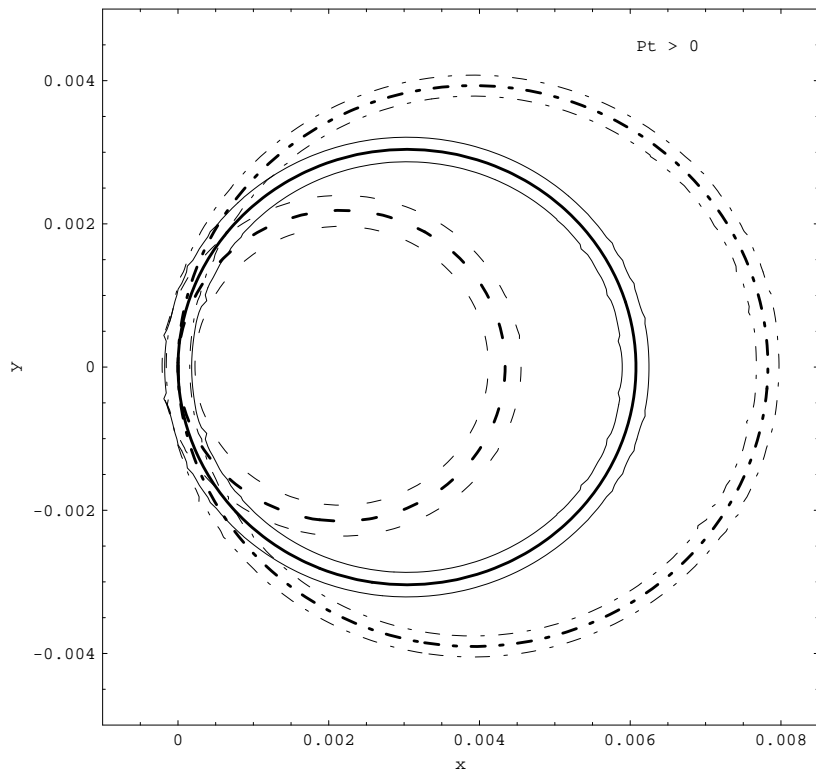


Figure 10: Contour plots as in figure 9 with  $x = d_{\gamma\gamma}$  and  $y = \bar{d}_{\gamma\gamma}$

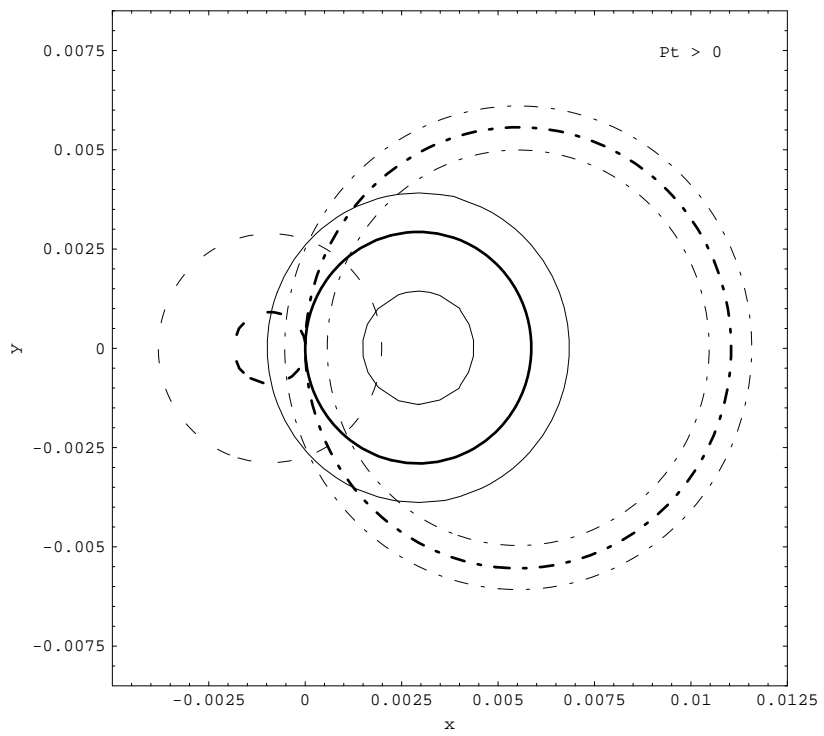


Figure 11: Contour plots as in figure 9 with  $x = d_{\gamma Z}$  and  $y = \bar{d}_{\gamma Z}$

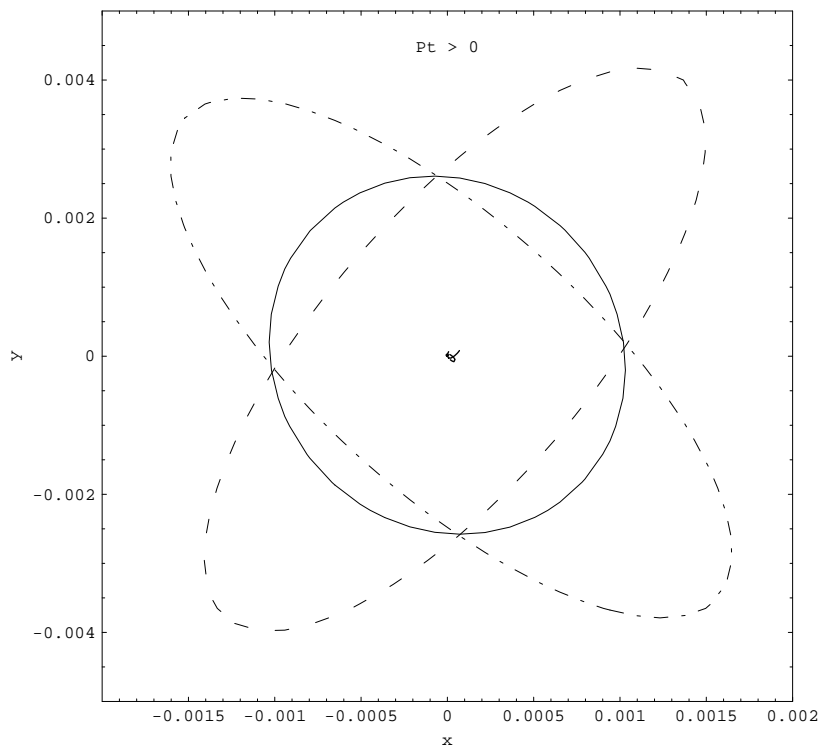


Figure 12: Contour plots as in figure 9 with  $x = \bar{d}_{\gamma\gamma}$  and  $y = \bar{d}_{\gamma Z}$

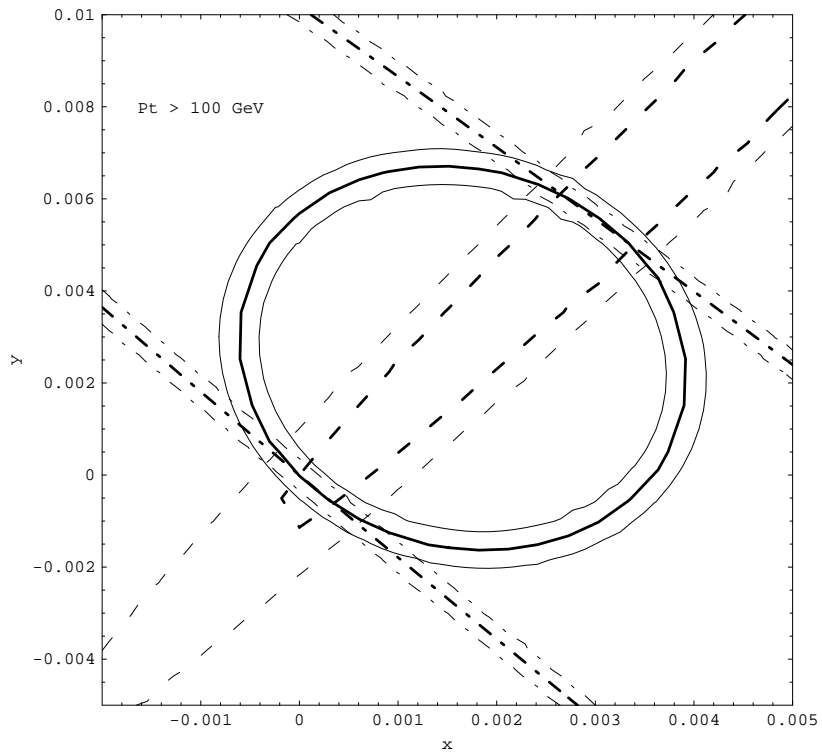


Figure 13: Contour plots as in figure 9 with  $x = d_{\gamma\gamma}$  and  $y = d_{\gamma Z}$ , with  $p_T^e > 100$  GeV (no restriction on the final electron angle  $\theta_e$ ).

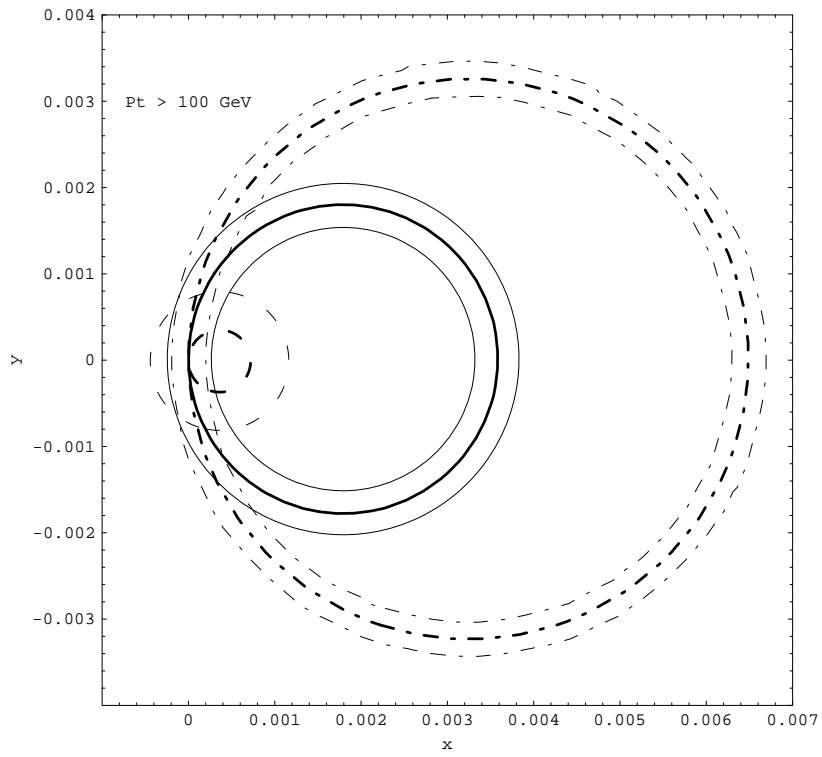


Figure 14: Contour plots as in figure 13 with  $x = d_{\gamma\gamma}$  and  $y = \bar{d}_{\gamma\gamma}$ .



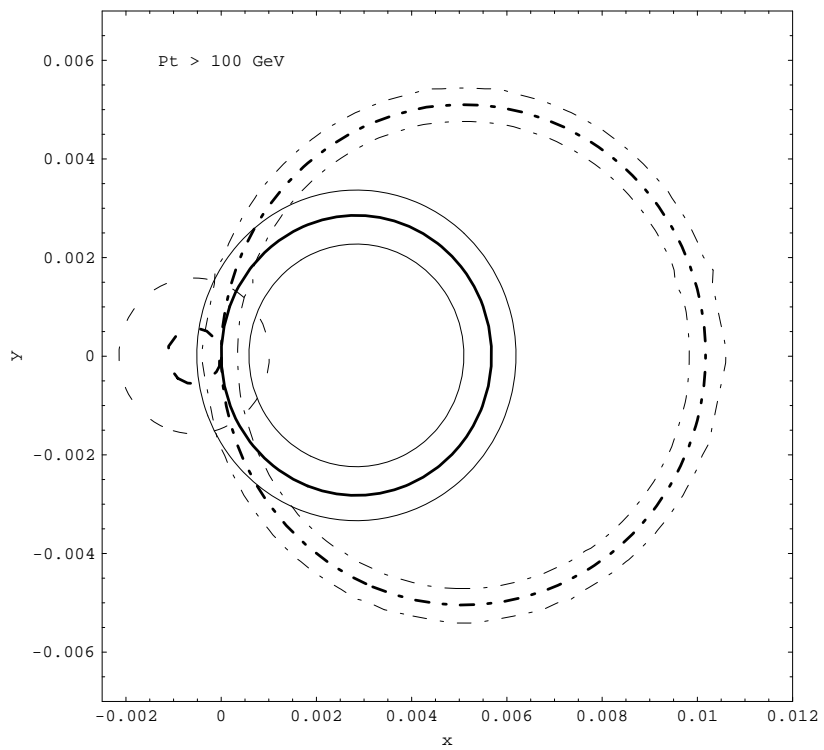


Figure 15: Contour plots as in figure 13 with  $x = d_{\gamma Z}$  and  $y = \bar{d}_{\gamma Z}$ .

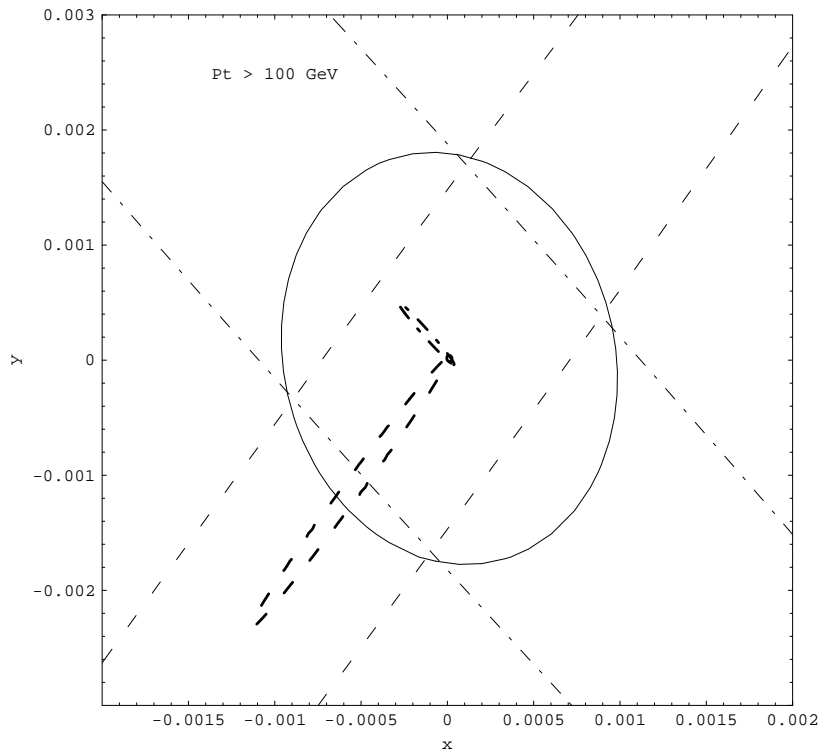


Figure 16: Contour plots as in figure 13 with  $x = \bar{d}_{\gamma\gamma}$  and  $y = \bar{d}_{\gamma Z}$ .